Picosecond time scale imaging of mechanical contacts

Thomas Dehoux [a,*], Oliver B. Wright [a], Roberto Li Voti [b]

[a] Division of Applied Physics, Graduate School of Engineering, Hokkaido University, Sapporo 060-8628, Japan
[b] Dipartimento di Energetica, Sapienza Università di Roma, Via A. Scarpa 16, Roma 00161, Italy

ARTICLE INFO

ABSTRACT

By means of an ultrafast opto-acoustic technique we study the nanoindentation of thin chromium films on sapphire substrates using a ceramic ball bearing. Acoustic pulses at ∼40 GHz returning from the film–indenter interface allow the film indentation profiles to be probed to sub-nanometer resolution over contact areas ∼25 μm in radius. The deformation of the films during loading is thereby revealed. Furthermore, thermal wave imaging of the contact at megahertz frequencies is simultaneously achieved.

© 2009 Elsevier B.V. All rights reserved.

1. Introduction

The trend for device miniaturization requires the development of characterization techniques for the mechanical properties of nanostructures, especially thin films. Nanoindentation has provided a means to measure both elastic and plastic properties [1]. The use of sharp probes, such as pyramidal indenters or the tips in atomic force microscopes (AFM), offers nanometer lateral resolution determined by the indenter radius [2]. Owing to the localized force, plastic deformation occurs immediately as the sample is indented. In contrast to the case of spherical indenters [3], these sharp-tip techniques cannot be used to separately study elastic and plastic behaviour. Plastic deformation leads to pile-up or sink-in near the edges of the contact, inducing errors in the measurement of hardness or elasticity [1]. To quantify such effects, AFM or electron microscope imaging of the indented surface can be performed after the indenter is withdrawn. However, this does not permit detailed measurement of plastic flow during loading.

Attention has therefore been focused on imaging during loading. In particular, ultrasonic imaging up to megahertz frequencies in contact mechanics allows access to the interfacial stiffness or the contact pressure [4–8]. However, with a resolution of the order of the acoustic wavelength (∼0.1 mm) at the typical frequencies used (∼30 MHz), one cannot effectively probe contacts of nanoscale thickness. In this paper we describe a profiling technique for nanoscale mechanical contacts that implements the generation and detection of ultrasound with ultrashort optical pulses [9–11],

offering acoustic frequencies up to and above 1 THz, sub-micron acoustic wavelengths, and ∼1 μm lateral resolution by optical focusing to a diffraction limited spot. Furthermore, we show how this technique provides access to thermal properties through imaging MHz variations in thermoreflectance.

2. Contact characterization

We prepared two samples consisting of polycrystalline Cr films of thicknesses 110 nm and 215 nm deposited by RF (radio frequency) sputtering on (0 0 0 1) sapphire substrates of thickness 0.8 mm. The samples lie horizontally on a rigid holder pierced with a 3.5 mm diameter hole for optical access. A sintered silicon nitride ball bearing of radius $R = 2.98$ mm is pressed against the Cr film using a high precision displacement stage. The load, monitored with a load cell, is stable to 5% during the experiments. Relevant physical properties are the longitudinal sound velocity V_n, Poisson's ratio v_n and Young's modulus E_n, with $n = i, f, s$ referring to the indenter, film and substrate, respectively. We use the following values: $V_i = 10.6$ km s^{-1}, $V_f = 6.65$ km s^{-1}, $V_s = 11.1$ km s^{-1}, $v_i = 0.29$, $v_f = 0.21$, $v_s = 0.23$, $E_i = 320$ GPa, $E_f = 280$ GPa and $E_s = 440$ GPa [10–12].

In order to study phonon transmission through a nanoscale heterogeneous interface, we used highly polished surfaces. The surface roughnesses of the films and the sphere were determined using an AFM with a 40 nm step. Typical line traces are shown in Fig. 1. From the AFM images, we determine the distributions of asperity heights for each sample, as plotted in Fig. 2. We obtain a good fit of these distributions to Gaussian functions. The rms roughnesses thus obtained, defined as one standard variation from
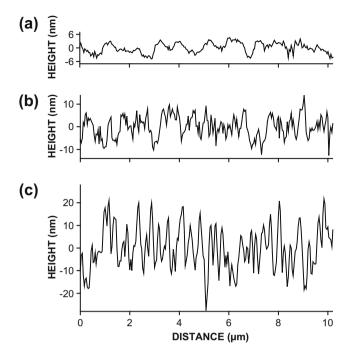

Fig. 1. Typical AFM traces measured in: (a) the 110 nm Cr film, (b) the 215 nm Cr film and (c) the Si_3N_4 spherical indenter.
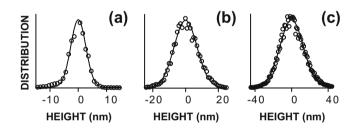

Fig. 2. Measured (circles) asperity height probability distributions and Gaussian function fit (lines) for: (a) the 110 nm Cr film, (b) the 215 nm Cr film and (c) the Si_3N_4 spherical indenter.

the mean value, are $\sigma_{f1} = 3$ nm, $\sigma_{f2} = 7$ nm and $\sigma_i = 13$ nm for the 110 nm film, the 215 nm film and the indenter, respectively. The rms roughness of the bare sapphire substrate (not shown) is $\sim$1 nm. Since we measured distributions that are Gaussian, we can neglect asymmetric effects such as skewness and tortuosity [13]. Therefore the asperity geometry and the behaviour of the contact can be predicted by standard theories [14–16].

The generic Hertz theory describes the contact between a rigid sphere of radius R and a flat elastic half-space, pressed onto each other with a force F. The pressure at the contacting interface $p(r)$ is distributed over a circular contact area of radius a as follows [14]:

$$p(r) = p_0 \left[1 - \left(\frac{r}{a} \right)^2 \right]^{1/2}, \tag{1}$$

where r is the radial coordinate and p_0 is the maximum pressure at the center of the contact ($r = 0$):

$$p_0 = \frac{3F}{2\pi a^2}. \tag{2}$$

At such a pressure p_0, the rigid sphere penetrates into the sample down to a depth δ_0 at $r = 0$:

$$\delta(r = 0) = \delta_0 = \frac{a^2}{R}. \tag{3}$$

To describe accurately our indentation conditions, we need to include the elasticities of the Cr film and Si_3N_4 sphere. Since the Cr film thickness is very thin compared to a (typically $\sim$30 μm in our experiment), we assume the pressure distribution at the surface of the substrate is not modified by the metal layer. So we consider the simplified system of a Al_2O_3 half-space indented by a Si_3N_4 sphere [14]:

$$a = \left(\frac{3FR}{4E^*} \right)^{1/3}, \tag{4}$$

where

$$E^* = \left[\frac{1 - v_i^2}{E_i} + \frac{1 - v_s^2}{E_s} \right]^{-1} \tag{5}$$

is the effective Young modulus accounting for the elasticities of both the indenter and the substrate. Empirical models [17,18] were proposed to modify E^* to include the influence of the Cr film. In our case of a soft layer on a hard substrate,

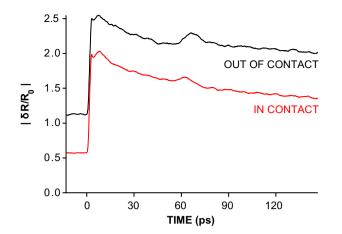$$\frac{(1 - v_s)E_f}{(1 - v_f)E_s} = 0.6 < 1, \tag{6}$$

the value of a is expected to be slightly (by less than 5%) larger compared to the no-layer case [19]. As seen from Eqs. (2) and (3), the contact pressure should then decrease, and the total indentation depth should increase accordingly. This relatively small effect is not considered here. The quantity δ_0 of Eq. (3) is in this case not the indentation of the Cr film, but the approach of distant points in the normal direction of the whole Al_2O_3/Si_3N_4 system.

The surface roughness may also modify the pressure distribution and prevent the application of Hertz theory. Provided the scaled roughness $\alpha = \sigma/\delta_0 \ll 1$, where $\sigma = (\sigma_f^2 + \sigma_i^2)^{1/2}$ is the combined roughness, Hertz theory remains valid [14]. In the present case, $\sigma = 15$ nm for the rougher film and $\delta_0 \approx 180$ nm at the lowest load $F = 1.1$ N. So $\alpha < 0.08 \ll 1$, and Hertz theory applies increasingly well as the load increases.

3. Picosecond ultrasonics

Picosecond longitudinal acoustic pulses are generated in the Cr films at the Al_2O_3–Cr interface with linearly polarized pump pulses of duration 200 fs from a Ti:Sapphire mode-locked laser (with a repetition rate of 80 MHz, a wavelength of 810 nm and a pulse energy of 0.5 nJ). The optical pump reflectance at this interface is 0.5. The pump light is chopped at a frequency of 1.1 MHz for synchronous lock-in detection. The in-phase transient optical reflectance change at the Al_2O_3–Cr interface $\delta R(t)/R_0$, where $R_0 \approx 0.6$ is the optical probe reflectance, is measured with frequency-doubled circularly-polarized probe pulses of wavelength 405 nm and pulse energy 0.06 nJ as a function of the time delay t between the pump and probe pulses. The pump and probe beams are both focused on the Al_2O_3–Cr interface with a $50\times$ microscope objective to provide a lateral resolution of $\sim$1 μm. The objective is laterally scanned in the plane of the interface to probe different regions of the indented samples.

Fig. 3 shows $|\delta R(t)/R_0|$ (note that $\delta R(t) < 0$) for the load $F = 4.6$ N when probing at the center of the contact (bottom trace) and outside the contact (top trace) for the 215 nm sample. The 110 nm sample shows similar features. $|\delta R(t)/R_0|$ takes a lower value for delay times $t < 0$ in the case of contact. This is caused by thermally-induced changes in $\delta R(t)/R_0$ at the chopping frequency, discussed in Section 4. At $t = 0$ we observe a positive peak due to the excitation and relaxation of hot electrons in the Cr film. It is followed by a slow decrease owing to heat diffusion. At the maximum delay time we probe, $\tau = 150$ ps, the diffusion length in Cr is $\mu \sim (2\kappa\tau/C)^{1/2} = 94$ nm, where $\kappa = 94$ W m^{-1} K^{-1} and $C = 3.2 \times 10^6$ J m^{-3} K^{-1} are
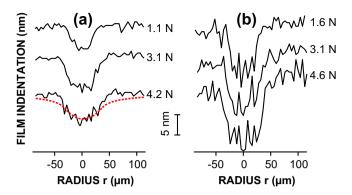
Fig. 3. $|\delta R(t)/R_0|$ for the load $F = 4.6$ N when probing at the center of the contact (bottom trace) and outside the contact (top trace) in the 215 nm sample.

Fig. 4. (a) Film indentation vs. the radial coordinate r at different loads in the 110 nm sample. Comparison between experiment (solid lines) and theory (dashed line) for $F = 4.2$ N. (b) Film indentation vs. r in the 215 nm sample.

the thermal conductivity and heat capacity of single crystal Cr, respectively [11]. Since μ is smaller than the film thickness, the picosecond-time-scale temperature variation at the contacting interface is not significant. Indeed in experiment, the background thermal decay does not depend on the contact (see Fig. 3). In what follows, we therefore do not consider picosecond-time-scale heat flow in the analysis of the mechanical contact.

Initially a hydrostatic longitudinal stress field is generated in the Cr over a depth $\sim$20 nm determined by the $\sim$15 nm optical absorption depth [20] at the pump wavelength and by the $\sim$15 nm electron diffusion depth [11]. The acoustic impedances of Cr and Al_2O_3 are such that the acoustic strain reflection coefficient at the film–substrate interface is almost zero. This results in two unipolar compressive longitudinal acoustic pulses of typical frequency 40 GHz and wavelength 170 nm being launched perpendicular to the film–substrate interface in opposite directions [21]. The acoustic strain pulse in the Cr film is reflected from the Cr film surface (or film–indenter interface), and is detected at the film–substrate interface, giving rise to the echoes at $t = \tau \sim 65$ ps in Fig. 3 (and at $t = \tau \sim 30$ ps in the 110 nm sample). Only one echo is detected because of the acoustic impedance matching at the Al_2O_3–Cr interface. The second acoustic pulse is transmitted into the substrate, and produces oscillations in $\delta R(t)/R_0$ at the Brillouin frequency $\sim$100 GHz [21]. Al_2O_3 has been chosen for its relatively high sound velocity (11.1 km/s) and low photoelastic constant p_{12} (-0.03 at the probe wavelength) in order to minimize these oscillations. Due to transmission through the film–indenter interface and scattering on the asperities, the height of the acoustic echo is reduced in contact. This phenomenon, analyzed with a proper calibration, allows the determination of the contact pressure [4,7,8].

A distinctive characteristic of picosecond ultrasonics is the ability to extract the nanoscale film indentation $\Delta h = h_0 - h = h_0 - V_f \tau/2$ from the echo arrival time $t = \tau$ and the film thickness h_0 out of contact. Thereby the deformation of the film is monitored during the indentation process. The indentations Δh obtained in the 110 nm and 215 nm samples are plotted as a function of the radial coordinate r in Fig. 4a and b, respectively. The radius of the indented region increases with load, as described by Eq. (4). The observed spikes show correlation at the different applied loads, which points to the influence of the surface roughness. The indentation profiles in the thicker Cr film appear to be deeper and more sensitive to the indenter roughness. In order to confirm this observation, further measurements were performed.

The load F is plotted against maximum indentation (at $r = 0$) in Fig. 5a for a first load–unload cycle (squares and triangles, respec-
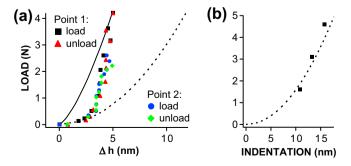
tively) in steps lasting 10 min in the 110 nm sample. A second load–unload cycle (circles and diamonds, respectively) performed at another location (not previously indented) shows the same trend, demonstrating the reproducibility of the experiment. The micro-hardness $H = 19$ GPa of RF sputtered Cr films of thickness $\sim$100 nm has been determined by Vickers indentation in Ref. [22]. For soft metals, this value corresponds to a yield stress in compression of $\approx$0.36$H = 7$ GPa [14]. We estimate the maximum pressure $p_0 = 1.6$ GPa at the highest load $F = 4.6$ N from Eq. (2). Thus the loading of the film is not sufficient for the bulk of the Cr to yield. The loading and unloading curves are nearly identical, as expected in the elastic regime.

We now compare the measured indentation Δh at $r = 0$ with the theory of indentation of a thin film on a rigid substrate by a rigid sphere [23]:

$$F = \frac{\pi(1 - v_f)RE_f\Delta h^2}{(1 + v_f)(1 - 2v_f)h_0}. \tag{7}$$

As seen in Fig. 5a for the 110 nm film, this model (dashed line) provides a reasonable estimate of the indentation at the lowest loads ($F < 0.5$ N). However, the measured Δh is smaller than that predicted at the highest loads, owing to the deformation of both the indenter and the substrate. The indentation at $r = 0$ in the 215 nm film corresponding to Fig. 4b (averaged over three points in the center of the contact) shows very good agreement with this theory, as depicted in Fig. 5b. This is presumably due to the lesser role played by the indenter and substrate elasticities for the thicker film [24].

To account for the elasticity of the substrate, one must determine the stresses resulting from an axisymmetric static load distribution on a finite region of the free surface, namely, the Boussinesq

Fig. 5. (a) Maximum indentation measured for load–unload cycles in the 110 nm sample (solid symbols) compared with theory for a rigid (dashed line) and an elastic (solid line) substrate. (b) Maximum indentation measured in the 215 nm sample (squares) compared with theory for a rigid substrate (dashed line).

problem [24,25]. The use of Hankel transforms reduces the formulation of this problem to a system of ordinary differential equations. The detailed solution for an arbitrary pressure distribution is given in Ref. [26]. Here we assume that the pressure distribution $p(r)$ at the contacting interface is not perturbed by the Cr film and remains Hertzian [27], as described in Eq. (1). The Hankel transform of order zero for $p(r)$ is:

$$\tilde{p}(\xi) = \int_0^{+\infty} p(r) r J_0(\xi r) dr = p_0 \left[-\frac{\cos(\xi a)}{\xi^2} + \frac{\sin(\xi a)}{a\xi^3} \right] \quad (8)$$

where J_0 is the zeroth order Bessel function of the first kind. Introducing Eq. (8) into the explicit expressions given in Ref. [26] allows us to calculate the Cr film indentation Δh. We compare this result (solid line) with the measured Δh in Fig. 5a. This second approach provides an asymptotic description of the indentation at high loads, when the influence of the substrate's elasticity is greatest. For this reason, it cannot be applied to describe the indentation of the 200 nm film since the high load limit is not reached for the range of loads we used for this sample. To represent Δh over the whole range of loads applied, the increasing participation of the substrate with increasing load should be introduced.

The second model for the indentation of an elastic layer resting on an elastic substrate also describes the radial deformation of the film. Since the predicted indentation matches the data well for the 110 nm film at high loads, we compare the indented profiles for the load $F = 4.2$ N in Fig. 4a. Good agreement is observed. When comparing with theory, the measured profile seems to bulge slightly at the edges of the contact area. This suggests the pressure distribution at the contacting interface is modified by the presence of the film.
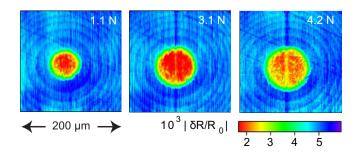
4. MHz thermoreflectance

We also image the contact area in two spatial dimensions over a $200 \times 200 \ \mu m^2$ region with step 1 μm, as shown for the example of $t = 40$ ps for the 110 nm sample in Fig. 6. Newton's rings [28] are visible owing to the modulated optical absorption at the pump wavelength $\lambda_{pp} = 810$ nm. They appear at a spacing determined by thickness variations Δd of the ball-film air gap for which

$$\Delta d = \frac{m\lambda_{pp}}{2} \quad (9)$$

for the mth ring. Thereby we measure Δd outside the contact area.

It is important to check if substrate bending affects these measurements. For a substrate of thickness $h_s = 0.8$ mm and for a sample holder pierced with a hole of radius $a_h = 1.8$ mm, plate theory can be applied [29]. The flexural rigidity of the sample is given by

$$D = \frac{E_s h_s^3}{12(1 - v_s^2)}. \quad (10)$$

Solving the equations of equilibrium for a simply supported circular geometry under a concentrated force F applied at $r = 0$ leads to the following expression for the maximum deflection at the center of the sample:

$$h_d = \frac{F a_h^2}{16\pi D} \frac{3 + v_s}{1 + v_s}. \quad (11)$$

For the maximum load $F = 4.6$ N, $h_d = 40$ nm. Since $h_d \ll a_h$, the curvature of the sample is negligible.

We therefore calculate the gap predicted by Hertz theory for a Al_2O_3 half-space. The Cr layer is not considered since its deformation, measured at ∼5 nm, is negligible compared to that of sapphire: $\delta_0 \approx 500$ nm at the maximum load $F = 4.6$ N. When the load F is applied, both the sphere and the sample are deformed. The sum of the deformations of each solid is

$$\delta = \frac{\pi p_0}{4E^* a}(2a^2 - r^2) \quad (12)$$

in contact, and

$$\delta = \frac{p_0}{2E^* a} \left[(2a^2 - r^2) \sin^{-1}\left(\frac{a}{r}\right) + ar\sqrt{1 - \frac{a^2}{r^2}} \right] \quad (13)$$

out of contact [14]. The position of the sphere surface during loading is described by the equation of the sphere penetrating into the sample by a depth δ_0:
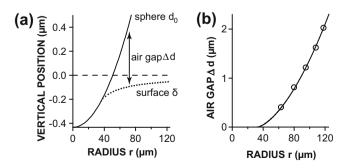
$$d_0 = R - \sqrt{R^2 - r^2} - \delta_0. \quad (14)$$

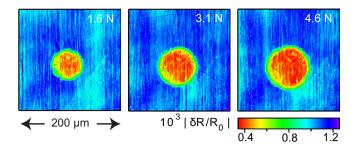During loading, the gap thickness becomes

$$\Delta d = d_0 - \delta. \quad (15)$$

The position of the indenter and the deformed surface of the sample are shown in Fig. 7a. We compare the predicted gap thickness with the measurement from the Newton's rings. The result for $F = 3.1$ N is plotted in Fig. 7b. Good agreement is found, confirming that the sample bending does not significantly affect the indentation process for $F < 4.6$ N. Fig. 8 shows the thermoreflectance image data for the 215 nm sample. As predicted for thicker films, no residual pump light penetrates through the Cr in the air gap, and so no Newton's rings are observed.
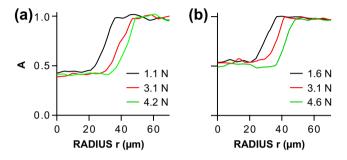
An offset is observed in the transients in Fig. 3 due to the modulated temperature change δT at the chopping frequency. This thermoreflectance contribution dominates the variation observed in Figs. 6 and 8. The contact size increases with F, in accord with Hertz theory [14]. Results for $|\delta R(t)/R_0|$ in both samples are compared in Fig. 9 at $t = -10$ ps, a time when only the thermal effects contribute. Due to the use of laser pulse trains, thermal harmonics of the laser repetition frequency also have an influence at the chopping frequency [30]. The normalized amplitude $A(r)$ of δT is shown. The contrast between in and out of contact is similar for both sam-

Fig. 6. $|\delta R(t)/R_0|$ images of the contact at $t = 40$ ps for the 110 nm sample.

Fig. 7. (a) Position of the Si_3N_4 sphere (solid line) and the deformed sample surface (dotted line). (b) Measured air gap thickness (circles) compared with Hertz theory (line).

Fig. 8. $|\delta R(t)/R_0|$ images of the contact at $t = 55$ ps for the 215 nm sample.

Fig. 9. Normalized amplitude of $|\delta R(t)/R_0|$ for $t < 0$ in (a) the 110 nm sample and (b) the 215 nm sample.

ple thicknesses. δT remains constant in the contact area, and is independent of load F. Yet for non-interacting asperities, overall force balance dictates that $S_r/S_0 = p_0/H$, where S_0 is the apparent contact area described by Hertz theory and S_r is the real contact area formed by the contacting asperities [31]. As S_r increases with increasing F, one might expect the contact thermal boundary resistance and δT to decrease in contact as F increases [31]. However, the observed F-independent thermal contrast suggests that this boundary resistance does not depend significantly on load over the range of loads probed. This anomalous behaviour could be explained by an enhanced heat transport through the interstitial air gaps. It might alternatively arise from the peculiarities of the three-dimensional solution of the heat diffusion equation for a system involving thermal boundary resistances at the film–substrate and film–indenter interfaces. The thermal measurement of the contact should offer a high sensitivity to the presence of the contact at lower F, whereas the acoustic measurements are more suitable at higher F.

5. Conclusion

In conclusion, we have applied picosecond ultrasonics to probe thin film properties during indentation by a sphere. Access to surface deformation during the indentation process provides a useful tool for investigating nanoscale plastic flow in or near the contact area. In addition, MHz thermoreflectance gives clear images of the thermal contact. In future, it would be interesting to extend the method to the study of films thinner than the picosecond-time-scale thermal diffusion length to probe high frequency heat transport through imperfect nanoscale interfaces. The use of an acousti-

cally mismatched film and substrate should allow the acoustic reflection from the indenter–film interface to be studied in more detail.

References

[1] G.M. Pharr, W.C. Oliver, Measurement of thin film mechanical properties using nanoindentation, Mater. Res. Soc. Bull. 17 (1992) 28–33.
[2] N.A. Burnham, R.J. Colton, Measuring the nanomechanical properties and surface forces of materials using an atomic force microscope, J. Vac. Sci. Technol. A 7 (1989) 2906–2913.
[3] M.V. Swain, Mechanical property characterisation of small volumes of brittle materials with spherical tipped indenters, Mater. Sci. Eng. A 253 (1998) 160–166.
[4] M. Masuko, I. Yoshimi, Measurement of contact pressures by means of ultrasonic waves, Ann. CIRP 17 (1969) 289–296.
[5] K. Kendall, R.F.S. Tabor, An ultrasonic study of the area of contact between stationary and sliding surfaces, Proc. R. Soc. Lond. A 323 (1971) 321–340.
[6] B.W. Drinkwater, R.S. Dwyer-Joyce, P. Cawley, A study of the interaction between ultrasound and a partially contacting solid–solid interface, Proc. R. Soc. Lond. A 542 (1996) 2613–2628.
[7] A.M. Quinn, B.W. Drinkwater, R.S. Dwyer-Joyce, The measurement of contact pressure in machine elements using ultrasounds, Ultrasonics 39 (2002) 495–502.
[8] T. Dehoux, O.B. Wright, R. Li Voti, V.E. Gusev, submitted for publication.
[9] C. Thomsen, H.T. Grahn, H.J. Maris, J. Tauc, Surface generation and detection of phonons by picosecond light pulses, Phys. Rev. B 34 (1986) 4129–4138.
[10] O.B. Wright, K. Kawashima, Coherent phonon detection from ultrafast surface vibrations, Phys. Rev. Lett. 69 (1992) 1668–1671.
[11] T. Saito, O. Matsuda, O.B. Wright, Picosecond acoustic phonon pulse generation in nickel and chromium, Phys. Rev. B. 67 (2003) 205421–205427.
[12] From Toshiba Materials Co. datasheet, 2008.
[13] N. Yu, A.A. Polycarpou, Contact of rough surfaces with asymmetric distribution of asperity heights, J. Tribol 124 (2002) 367–376.
[14] K.L. Johnson, Contact Mechanics, Cambridge University Press, 1985.
[15] J.A. Greenwood, J.B.P. Williamson, Contact of nominally flat surfaces, Proc. R. Soc. Lond. A 295 (1966) 300–319.
[16] Y. Kimura, Estimation of the number and the mean area of real contact points on the basis of surface profiles, Wear 15 (1970) 47–55.
[17] M.F. Doerner, W.D. Nix, A method for interpreting the data from depth-sensing indentation instruments, J. Mater. Res. 1 (1986) 601–609.
[18] R.B. King, Elastic analysis of some punch problems for a layered medium, Int. J. Solid Struct. 23 (1987) 1657–1664.
[19] H.Y. Yu, S.C. Sanday, B.B. Rath, The effect of substrate of the elastic properties of films determined by the indentation test – axisymmetric Boussinesq problem, J. Mech. Phys. Solid 38 (1990) 745–764.
[20] D. Lide, CRC Handbook of Chemistry and Physics, CRC Press, Boca-Raton, 1999.
[21] O.B. Wright, Laser picosecond acoustics in double-layer transparent films, Opt. Lett 20 (1995) 632–634.
[22] W. Lu, K. Komvopoulos, Nanomechanical and nanotribological properties of carbon, chromium, and titanium carbide ultrathin films, J. Tribol. 123 (2001) 717–724.
[23] M.J. Jaffar, A general solution to the axisymmetric frictional contact problem of a thin bonded elastic layer, Proc. Inst. Mech. Eng. 211 (1997) 549–557.
[24] H.Y. Yu, S.C. Sanday, B.B. Rath, The effect of substrate on the elastic properties of films determined by the indentation test – axisymmetric Boussinesq problem, J. Mech. Phys. Solid 38 (1990) 745–764.
[25] J.W. Harding, I.N. Sneddon, The elastic stresses produced by the indentation of the plane surface of a semi-infinite elastic solid by a rigid punch, Proc. Camb. Phil. Soc. 41 (1945) 16–26.
[26] J. Li, T.-W. Chou, Elastic field of a thin-film/substrate system under an axisymmetric loading, Int. J. Solid Struct. 34 (1997) 4463–4478.
[27] S. Math, V. Jayaram, S.K. Biswas, "Deformation and failure of a film/substrate system subjected to spherical indentation: Part I. Experimental validation of stresses and strains derived using Hankel transform technique in an elastic film/substrate system, J. Mater. Res. 21 (2006) 774–782.
[28] A. Cameron, R. Gohar, Theoretical and experimental studies of the oil film in lubricated point contact, Proc. R. Soc. Lond. A 291 (1966) 520–536.
[29] S. Timoshenko, Theory of Plates and Shells, McGraw-Hill, 1940.
[30] A.J. Schmidt, X. Chen, G. Chen, Pulse accumulation, radial heat conduction, and anisotropic thermal conductivity in pump-probe transient thermoreflectance, Rev. Sci. Instrum. 79 (2008) 114902.
[31] C.V. Madhusudana, Thermal Contact Conductance, Springer, New York, 1996.